Physica Scripta

INCLUSIVE PUBLISHING TRUSTED SCIENCE

PURPOSE-LED PUBLISHING™

PAPER • **OPEN ACCESS**

Mechanical-stage-free ultrafast pump–probe setup via dynamic holographic beam steering

To cite this article: Gamze Kaya 2026 *Phys. Scr.* **101** 455402

View the article online for updates and enhancements.

You may also like

- High power, high repetition rate laser-based sources for attosecond science
F J Furch, T Witting, M Osolodkov et al.
- Development and demonstration of table-top synchronized fast-scan femtosecond time-resolved spectroscopy system by single-shot scan photo detector array
Atsushi Yabushita, Chih-Hsien Kao, Yu-Hsien Lee et al.
- A modified pump–probe method for sensitive measurement of optical nonlinearity
Wenfa Zhou, Junyi Yang, Xingzhi Wu et al.

This content was downloaded from IP address 193.255.97.61 on 18/11/2026 at 16:05

Physica Scripta

Check for updates

OPEN ACCESS

RECEIVED
30 August 2026

REVISED
15 October 2026

ACCEPTED FOR PUBLICATION
29 October 2026

PUBLISHED
6 November 2026

Original content from this work may be used under the terms of the Creative Commons Attribution 4.0 licence.

Any further distribution of this work must maintain attribution to the author(s) and the title of the work, journal citation and DOI.

PAPER

Mechanical-stage-free ultrafast pump–probe setup via dynamic holographic beam steering

Gamze Kaya*

Department of Electricity and Energy, Vocational School of Technical Sciences, Canakkale Onsekiz Mart University, Canakkale, Turkiye
* Author to whom any correspondence should be addressed.

E-mail: gamzekaya@comu.edu.tr

Keywords: ultrafast pump–probe spectroscopy, holographic beam steering, all-optical delay line, ultrafast optics, spatiotemporal control

Abstract

Conventional ultrafast pump–probe setups suffer from spatial walk-off, beam pointing instability, and vibrational noise due to mechanical translation stages. To overcome these limitations, we introduce an all-optical, mechanical-stage-free holographic pump–probe technique. Utilizing a spatial light modulator, we spatially multiplex a single femtosecond beam into concentric pump and probe channels. The pump beam is holographically steered across a stationary silica wedge, translating lateral displacement into precise optical path length variations without any mechanical movement. To suppress lateral walk-off and maintain stable spatiotemporal overlap, a f 4 optical relay configuration is integrated to compensate for the angular deviation induced during beam steering. This automated setup successfully executes a continuous 2.3 ps temporal scan with a 4.6 fs temporal step size. The system performance is experimentally validated through optical cross-correlation measurements and quantitative centroid-tracking analysis of beam overlap stability.

1. Introduction

Ultrafast pump–probe spectroscopy is a foundational technique for observing and controlling transient phenomena on the femtosecond and picosecond timescales [1–4]. Recently, this technique has become indispensable for unraveling complex nanoscale physical phenomena, such as the dynamics of various polariton species including plasmon, phonon, and exciton polaritons [5, 6], moiré physics [7, 8], exotic spin textures [9], and complex many-body effects [10]. Furthermore, it is heavily utilized to track photoinduced insulator-to-metal transitions in strongly correlated materials like VO2 [11, 12] and interlayer electron–hole tunneling dynamics in van der Waals heterostructures, such as WSe2/WS2 [13, 14]. Despite its widespread applications, traditional pump–probe setups are inherently bottlenecked by mechanical translation stages. These moving parts inevitably introduce spatial walk-off, beam pointing instability, and vibrational noise, which are critical flaws when interrogating highly sensitive, nonlinear processes that require perfect spatial overlap over varying temporal delays [15]. Recent comprehensive reviews on state-of-the-art ultrafast spectroscopy emphasize that minimizing mechanical and thermal drift is crucial; these physical fluctuations severely compromise the precise spatiotemporal alignment and synchronization required to capture sensitive, nanoscale light–matter interactions [16].

To bypass these mechanical constraints, researchers have increasingly turned to dynamic spatial beam shaping and all-optical pulse control [10, 17–22]. Holographic beam shaping using spatial light modulators (SLMs) has emerged as a transformative tool in ultrafast optics, operating as a dynamic phase retardation map capable of quasi-arbitrary sculpting of the laser intensity distribution [23]. Unlike amplitude modulation techniques that inevitably involve significant loss of laser energy, SLMs perform wavefront (phase) modulation. While avoiding the severe intrinsic losses of amplitude masks, this approach is fundamentally limited by the first-order diffraction efficiency and higher-order scattering, yet it adequately preserves the pulse energy required for highly sensitive nonlinear processes [10, 24]. Furthermore, SLMs

© 2026 The Author(s). Published by IOP Publishing Ltd

provide unparalleled dynamic reconfigurability, granting the agility to seamlessly adapt the laser beam shape, compensate for depth-dependent spherical aberrations, and rectify experimental distortions—all without the need for physical moving parts [10, 25, 26]. This mechanical-stage-free approach builds upon recent demonstrations of dynamic spatiotemporal beam control using SLMs [27, 28] to significantly refine the stability and precision of conventional pump–probe methodologies previously employed for tracking nonadiabatic molecular alignment and strong-field ionization dynamics [29–32].

Although the potential of SLMs for diffraction-based pulse shaping has been demonstrated [33, 34], their application as a complete replacement for physical moving parts in high-resolution temporal scanning remains an evolving frontier. Recent advancements have sought to improve signal-to-noise ratios and dispersion compensation [2, 3]; nevertheless, achieving entirely non-mechanical temporal scanning without introducing diffractive walk-off remains a persistent challenge. While SLM beam steering, 4 f optical relays, and static wedge delays are well-established concepts individually, in this study, we introduce their specific integration into a novel hybrid holographic delay scheme that entirely eliminates the need for mechanical translation stages in ultrafast pump–probe spectroscopy. We employ an SLM not only to spatially multiplex and precisely overlap the pump and probe beams at the focal plane, but crucially, to execute a fully all-optical temporal scan. By combining a static material-based coarse delay with high-resolution holographic steering—laterally sweeping the beam across a stationary glass wedge via computer-generated holograms—we precisely scan the temporal delay. Furthermore, to effectively mitigate the lateral walk-off inherent in holographic angular steering, a 4 f optical relay imaging system is integrated into the architecture. To validate the precision and stability of this non-mechanical architecture, we utilize it to perform rigorous structural characterizations, specifically tracking spatial pointing stability and measuring temporal resolution via optical cross-correlation in a β-Barium Borate (BBO) crystal. Given their high sensitivity to precise spatiotemporal overlap, non-collinear sum-frequency and second-harmonic generation processes serve as a rigorous optical testbed for validating our setup. Through precise measurement of these parameters, we demonstrate that this configuration provides high-stability spatiotemporal control over light–matter interactions within a shared focal volume, demonstrating the suitability of the architecture for stable ultrafast optical diagnostics.

The primary novelty of the present work lies in the integration of holographic beam steering, static wedge-based optical delay generation, and 4 f relay compensation into a unified all-optical pump–probe architecture capable of executing mechanical-stage-free temporal scanning while preserving stable spatial overlap at the interaction region. Specifically, the main contributions of this study are: (i) the implementation of a fully all-optical temporal scanning mechanism based on lateral holographic beam steering across a stationary silica wedge, (ii) the incorporation of a 4 f relay imaging system to compensate for steering-induced angular deviation and suppress lateral walk-off, and (iii) the experimental validation of spatiotemporal stability through quantitative centroid tracking and nonlinear SHG/SFG optical cross-correlation measurements. Together, these elements establish a compact and alignment-stable alternative to conventional mechanically translated pump–probe delay systems.

2. Methodology

As schematically illustrated in figure 1, the experimental methodology relies on precise spatiotemporal wavefront engineering utilizing a liquid-crystal-on-silicon SLM (LCOS-SLM, Hamamatsu) as the central engine for diffractive beam splitting and all-optical temporal scanning. The system is driven by a Ti:Sapphire regenerative amplifier delivering $\sim$50 fs pulses centered at 800 nm with a 1 kHz repetition rate and approximately 1 mJ of pulse energy. A single expanded input beam (0.33 cm diameter) is spatially multiplexed onto the SLM's active area, thereby bypassing the need for vibration-prone mechanical translation stages. This configuration divides the incident beam into concentric pump and probe channels with a 50/50 energy split. Accounting for the SLM's first-order diffraction efficiency and subsequent optical transmission losses, this yields a final pulse energy of approximately 180 μJ per channel at the interaction region.

The inner region of the beam serves as the probe channel, which propagates directly to the interaction region to establish the zero-delay reference point for the cross-correlation measurements. The outer annular region acts as the pump channel and is programmed with a dynamic composite phase mask. The composite phase mask is computed by mathematically superimposing the phase profiles of a focusing Fresnel lens, a blazed splitting grating, and an off-axis carrier grating wrapped modulo 2π. To maintain strict diffraction efficiency and avoid spatial aliasing, the steering geometry of this digital phase mask is optimized with an effective focal length of approximately 2000 mm.

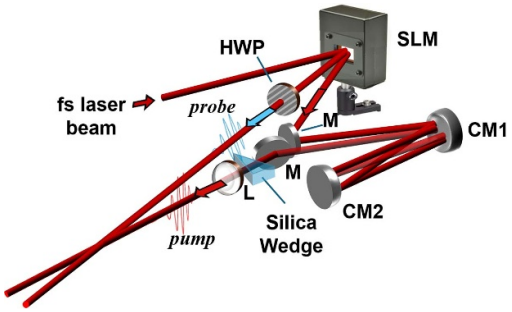


Figure 1. Schematic of all-optical, mechanical-stage-free holographic pump–probe setup. An LCOS-SLM spatially multiplexes the input beam into a central probe and an outer annular pump channel. The pump beam is holographically steered across a stationary 5° silica wedge, enabling high-resolution, mechanical-free temporal scanning. To mitigate lateral walk-off, a f 4 optical relay system actively compensates for the angular deviation induced by the steered beam. Together with large-aperture optics, this configuration ensures highly stable spatiotemporal overlap within the target medium. (CM: Concave Mirror, M: Flat Mirror, L: Lens, HWP: Half-Wave Plate). The 4 f configuration ensures angular compensation and preserves spatial overlap during holographic scanning.

By sequentially varying the spatial period of a superimposed blazed grating, the SLM imparts a precise lateral tilt angle to the pump beam, holographically sweeping it across a stationary 5° silica wedge. This geometrical configuration directly translates lateral spatial displacement into optical path length variation without requiring any physical movement.

Importantly, the propagation of the 50 fs ultrashort pulses through the transmission elements—primarily the silica wedge—introduces only minimal dispersive broadening. The temporal pulse broadening was estimated using the standard Gaussian pulse propagation relation: $\tau_{\text{out}} = \tau_0\sqrt{1+(4\ln 2\cdot \text{GDD}/\tau_0^2)^2}$ where τ_0 is the initial pulse duration and GDD represents the accumulated group delay dispersion introduced by the optical material. Based on the dispersive properties of fused silica at 800 nm and the maximum optical propagation length within the 5° wedge geometry, the cumulative GDD remained below approximately 200 fs^2. While the cumulative GDD is low, the asymmetric pulse deformation typically induced by third-order dispersion (TOD) was also evaluated. Given the minimal thickness of the 5° fused silica wedge, the accumulated TOD remains well below the threshold required to distort 50 fs pulses, ensuring that the temporal envelope retains its symmetric Gaussian profile throughout the scan. Substituting this value into the above relation predicts a temporal broadening of less than 1 fs for the initial 50 fs pulses. Consequently, the effective pulse duration is preserved near the transform-limited regime throughout the holographic delay scan, maintaining the peak intensity required for nonlinear cross-correlation measurements without requiring additional external dispersion compensation. This result is also experimentally consistent with the SHG/SFG cross-correlation traces presented in figure 6, where no observable asymmetric temporal broadening or temporal distortion was detected across the full scan range.

The temporal delay introduced by the wedge-based holographic scanning geometry can be approximated by: $\Delta t = \frac{(n-1)\Delta x\tan(\theta)}{c}$ where (n) is the refractive index of fused silica at 800 nm, (Δx) is the lateral beam displacement across the wedge surface, (θ) is the wedge angle, and (c) is the speed of light in vacuum. Using a maximum lateral sweep distance of 17.1 mm and a wedge angle of 5°, the experimentally accessible temporal delay window was approximately 2.3 ps, consistent with the measured SHG/SFG cross-correlation calibration.

A critical challenge in holographic angular steering is the inherent lateral walk-off. To effectively mitigate this lateral walk-off, we implement a 4 f optical relay system rather than a standard single Fourier-transform mirror. This imaging setup precisely maps the spatial profile from the SLM plane onto the wedge, actively compensating for the induced angular deviation. Consequently, it ensures that the pump beam enters the final focusing objective parallel to the optical axis. To prevent the unmodulated zero-order beam and high-order diffractions from reaching the interaction region and introducing background noise, a precision spatial pinhole is positioned at the Fourier plane of the 4 f relay system. This ensures that only the desired first-order steered pump beam is transmitted to the final objective.

The pump and probe beams are independently focused into the interaction region using a decoupled 60 cm focal length geometry, with their intersection angle strictly adjusted to be less than 3 degrees. The LCOS-SLM operates at a 60 Hz frame rate. With an initial beam diameter of 0.33 cm and 1 mJ total energy, the incident peak fluence on the SLM is approximately 11.7 mJ cm^{-2}. Maintaining this operating fluence well below the typical damage threshold of the LCOS-SLM prevents thermal nonlinearities and

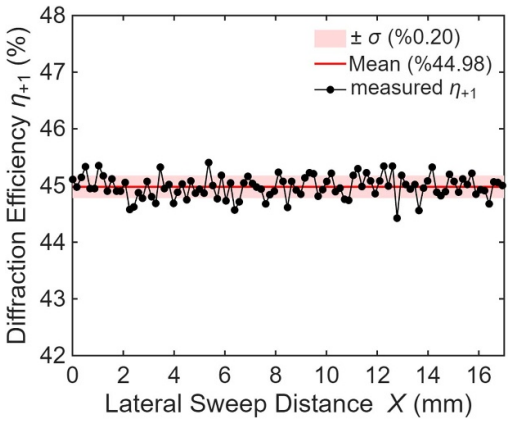


Figure 2. Measured +1st -order diffraction efficiency (η_{+1}) as a function of lateral sweep distance (x). The black markers represent the experimental data. The solid red line indicates the mean diffraction efficiency, while the shaded area corresponds to the standard deviation ($\pm\sigma$), demonstrating the exceptional spatial stability of the holographic sweep.

ensures long-term stability. An automated MATLAB-based control sequence executes the 500-point scan in 60–90 s by synchronizing hologram computation, SLM refresh cycles, and simultaneous data acquisition via a CCD camera and spectrometer.

3. Results and discussion

Traditional mechanical delay lines are inherently limited by physical acceleration, deceleration, settling times, and mechanical wobble/pitch of motorized stages, which significantly extend measurement durations and increase susceptibility to environmental fluctuations. Our all-optical hybrid architecture bypasses these physical constraints, demonstrating lateral pointing stability bounded within $\sim$14 μm over the full continuous scan. By operating as a pure instrumentation proof-of-concept validated via highly phase-sensitive SHG/SFG, this setup establishes the temporal and spatial baseline required for future transient absorption measurements on standard samples. Using the rapid acquisition sequence described in section 2, the seamless digital integration minimizes the impact of thermal drifts, ambient vibrations, and laser power fluctuations, providing a highly stable platform for ultrafast optical diagnostics.

A fundamental limitation of utilizing diffractive elements for dynamic beam steering is the introduction of lateral walk-off, which typically degrades spatial overlap at the focal plane. To quantitatively evaluate spatial overlap and pointing stability, the focal plane—where the pump and probe beams intersect—is magnified and imaged directly onto a CCD camera. Throughout the continuous temporal scan, we record and track the specific spatial coordinates (the X and Y centroids) of both the pump and probe beam profiles. Beam centroid coordinates are calculated using a dynamic, intensity-weighted center-of-mass algorithm across the two-dimensional (2D) pixel array. Specifically, the horizontal centroid is computed by summing the product of each pixel's x-coordinate and its intensity, normalized by the total integrated intensity of the entire beam profile, with an analogous calculation performed for the vertical centroid. This provides a precise metric for tracking micrometer-scale lateral drifts throughout the holographic scan. Beam centroid coordinates were initially determined in pixel units and subsequently converted into physical distances using the manufacturer-specified CCD pixel pitch of 3.45 µm.

Before evaluating the spatial overlap, the energetic consistency of the process was characterized. Figure 2 illustrates the stability of the holographic sweep as a function of lateral sweep distance. In this analysis of $N = 500$ independent measurements, the black markers represent the experimental data, the solid red line indicates the mean first-order diffraction efficiency (η_1) of 44.98%, and the shaded area corresponds to the standard deviation ($\pm\sigma$) of $\pm$0.20%. This exceptional statistical uniformity across the discrete spatial points confirms that the pump beam intensity remains constant throughout the temporal window, preventing power-induced artifacts during data acquisition.

To quantitatively evaluate the spatial pointing stability and the preservation of focal spot geometries during the all-optical temporal scanning sequence, the intensity distributions at the shared interaction region were systematically monitored and analyzed via the automated center-of-mass routine. Figures 3(a)–(c) illustrate the calibrated 2D spatial intensity profiles of the fundamental beams. Specifically, figure 3(a) shows the spatial profile of the stable, stationary probe beam, where its $1/e^2$

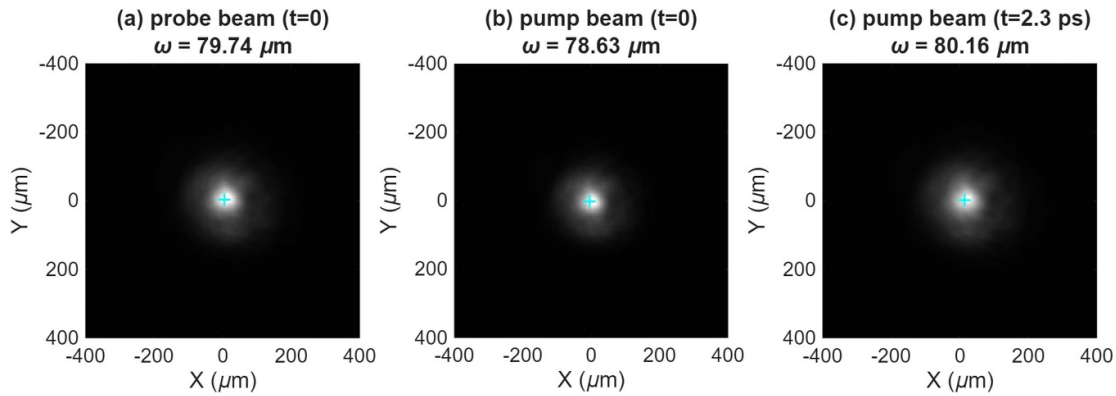


Figure 3. Two-dimensional (2D) spatial intensity profiles and measured parameters of the fundamental beams in the all-optical pump–probe system. (a) Spatial profile of the stable Probe beam at $t = 0$; and the beam radius ω is calculated as $\approx 80\,\mu$m. (b) Profile of the Pump beam at the reference $t = 0$ ($\omega \approx 73\mu$m). (c) Profile of the Pump beam at a 2.3 ps time delay and the beam size with $\omega \approx 85\,\mu$m and the spatial drift relative to the reference centroid are clearly visible. In all three panels, cyan-colored plus signs (+) represent the intensity-weighted centroid positions.

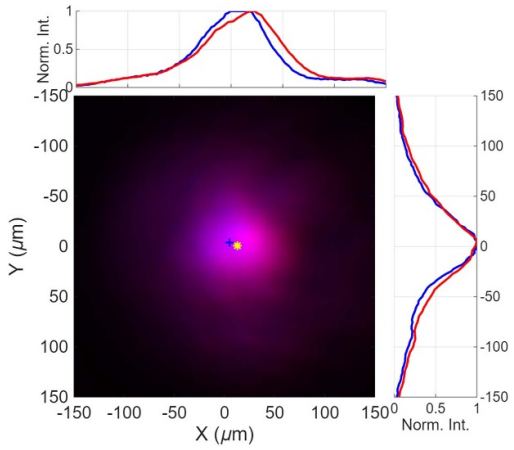


Figure 4. Multi-panel detailed analysis of the spatial overlap of the Pump and Probe beams at the critical crossing point ($t = 2.3$ ps). The center panel shows the overlaid normalized 2D intensity profiles of the two beams using RGB color synthesis; the Red channel represents the Pump beam ($t = 2.3$ ps), and the Blue channel represents the Probe beam ($t = 0$). The yellow star ($*$) indicates the Pump centroid, and the blue plus (+) indicates the Probe centroid. The horizontal graph above panel (d) shows the cross-sectional profiles (Normalized Intensity vs Distance) taken along the X -axis passing through the Probe centroid, while the vertical graph on the right shows the cross-sectional profiles (Normalized Intensity vs Negative Distance) taken along the Y -axis passing through the Probe centroid. Blue solid lines are the Probe profiles, and red solid lines are the Pump profiles. These cross-sections verify the micrometer-level precision of the overlap error at the main crossing point.

beam radius (ω_0) is calculated with a fitting uncertainty of ± 0.5 μm. Figures 3(b) and (c) display the profile of the pump beam at the reference delay ($t = 0$) and at the maximally steered delay ($t = 2.3$ps), respectively. The slight geometric expansion of roughly 1.5 μm arises naturally as the dynamically steered beam traverses differing optical path lengths through the angled silica wedge. The intensity-weighted centroid positions, marked by cyan-colored plus signs (+) in all panels, allow for clear visualization of the beam size expansion and the minimal spatial drift relative to the reference centroid. The experimental data confirms that the near-Gaussian beam profile and the intrinsic peak power requirements necessary for phase-sensitive nonlinear cross-correlation are robustly maintained without introducing severe diffractive spatial walk-off or structural deformation.

The effectiveness of the 4 f optical relay architecture in compensating for the angular deviation induced by digital blazed grating modulation is visually and numerically demonstrated in the multi-panel detailed analysis in figure 4. By overlaying the normalized 2D intensity profiles using RGB color synthesis—where the red channel represents the maximally delayed pump beam () and the blue channel represents the zero-delay probe beam (t =2.3 ps)—the shared focal area yields a highly symmetric, well-centered overlapping spatial envelope. Figure 4 further details this through cross-sectional profiles (Normalized Intensity vs Distance) taken along the x-axis and y-axis passing through the probe centroid. These cross-sections verify the micrometer-level precision of the overlap error at the main crossing point.

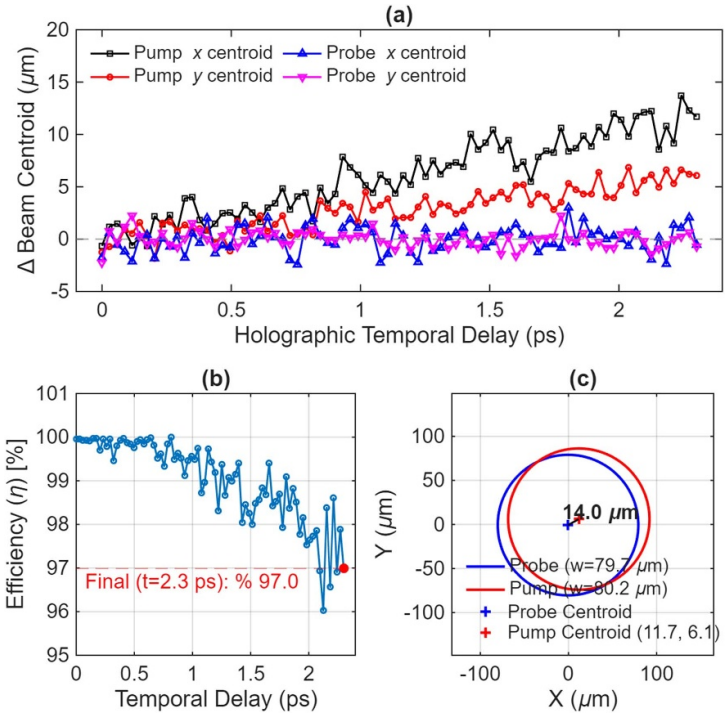


Figure 5. Quantitative analysis of spatial pointing stability and overlap efficiency during the holographic temporal scan. (a) Dynamic centroid displacement of the pump and probe beams within the probe-centered coordinate system over the 2.3 ps delay window. The black squares and red circles represent the pump beam x- and y-direction centroid drifts, respectively, while the blue upward triangles and purple downward triangles correspond to the probe beam centroid stability. (b) Instantaneous spatial overlap efficiency (η) calculated using the normalized two-dimensional overlap integral between the experimentally measured pump and probe intensity distributions. The overlap efficiency remains above 97.0% throughout the entire scan range, demonstrating excellent preservation of beam overlap despite the holographic steering process. (c) Two-dimensional spatial boundary contours of the pump and probe beams at the maximum temporal delay ($t = 2.3$ ps). The dashed black line indicates the final centroid separation distance of 14.0 μm, corresponding to approximately 15.1% of the near-Gaussian focal spot radius, confirming highly stable spatial overlap throughout the holographic delay scan.

The plotted profiles represent single-shot data captures, directly reflecting instantaneous spatial overlap quality. The minor discrepancies in decay rates and the centroid offset are not alignment errors, but rather physical asymmetries arising because the pump beam traverses a dynamic off-axis hologram and an angled wedge, unlike the on-axis stationary probe. The sub-pixel tracking of the respective centroids, indicated by the yellow star (*) for the pump and the blue plus (+) for the probe, reveals that the spatial deviation remains tightly bounded within the micrometer-scale stability regime across the entire 2.3 ps temporal window. This spatial stability firmly validates that the hybrid holographic delay line successfully bypasses the performance bottlenecks traditionally imposed by physical translation stages.

To quantitatively evaluate the spatial overlap between the pump and probe beams during the holographic temporal scan, a normalized 2D overlap integral was calculated from the experimentally recorded beam intensity distributions. The overlap efficiency was defined as the normalized spatial correlation between the pump intensity distribution ($I_{\mathrm{p}}(x,y)$ and the probe intensity distribution $I_{\mathrm{pr}}(x,y)$): $\eta = \frac{\iint I_{\mathrm{p}}(x,y), I_{\mathrm{pr}}(x,y), \mathrm{dxdy}}{\sqrt{(\iint I_{\mathrm{p}}^2(x,y), \mathrm{dxdy})(\iint I_{\mathrm{pr}}^2(x,y), \mathrm{dxdy})}}$ where ($\eta = 1$) corresponds to perfect spatial overlap. This metric provides a robust quantitative measure of the preservation of spatiotemporal beam overlap throughout the all-optical scanning process, while simultaneously accounting for beam drift and spatial profile deformation.

As shown in figure 5, an in-depth analysis of spatial pointing stability and overlap efficiency confirms the efficacy of the 4 f relay in compensating for the induced angular deviation. Figure 5(a) maps the dynamic shift of the beam centroids over the 2.3 ps holographic time delay; the pump beam exhibits tightly controlled lateral movement (Pump X drift indicated by a black line with squares, Pump Y drift by a red line with circles), while the probe beam maintains exceptional spatial stability with only ± 1 μm of noise (blue and purple lines with triangles). Figure 5(b) illustrates the instantaneous dynamic overlap efficiency (η, %), which starts at an optimal level of $\approx 100\%$ and consistently maintains a high value, dropping only to 97.0% at the end of the scan ($t = 2.3$ ps) due to minor drift and beam expansion. Finally, figure 5(c) maps the intersection of the 2D spatial boundaries—the intensity contours, revealing a final drift distance between the centers of only 14.0 μm (indicated by the dashed black line). Given

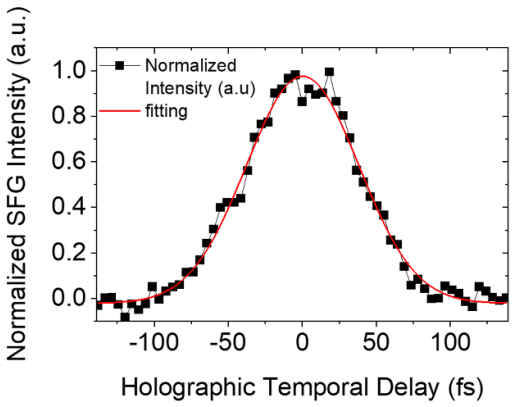


Figure 6. Experimental SHG/SFG optical cross-correlation trace used to validate the temporal precision and linearity of the holographic delay scanning mechanism. The normalized nonlinear signal generated in the BBO crystal is plotted as a function of the applied holographic temporal delay. The solid red curve represents the Gaussian fit applied to the experimental data. The extracted FWHM remains consistent with the expected convolution width of near-transform-limited ∼50 fs pulses, confirming negligible temporal broadening during holographic steering. The magnified 276 fs interaction region clearly resolves the discrete temporal sampling intervals, experimentally validating the highly linear 4.6 fs temporal sampling step achieved without mechanical translation. The blue dashed line, plotted on the secondary axis, represents the absolute phase difference, demonstrating the minimal divergence between calibration methods.

that the near-Gaussian beam focal spot radius is approximately 92.6 μm, this absolute spatial deviation represents a geometric shift of roughly 15.1%. Consequently, the decoupled pump and probe beams maintain a highly stable spatiotemporal overlap.

To rigorously confirm the temporal resolution and linearity of the all-optical scanning mechanism, an optical cross-correlation measurement serves as the definitive physical proof-of-concept. For this structural characterization, a thin nonlinear medium—specifically, a β -Barium Borate (BBO) crystal—is placed at the focal plane where the decoupled pump and probe beams intersect. The optical relay imaging system guarantees that the beams enter the 60 cm focusing objective parallel to each other, ensuring stable spatial overlap on the crystal.

Figure 6 presents the experimentally measured optical cross-correlation trace used to evaluate the temporal precision and linearity of the holographic delay scanning mechanism. The normalized SHG/SFG intensity generated within the BBO crystal was recorded as a function of the applied holographic temporal delay, producing the characteristic Gaussian-shaped cross-correlation envelope expected from the interaction of near-transform-limited femtosecond pulses.

The experimental trace was fitted using a Gaussian model, $I(t) = I_0 + A\exp[-((t-t_c)^2)/(2\sigma^2)]$, in order to evaluate the temporal consistency and stability of the all-optical scanning process. The Gaussian fit yielded a goodness-of-fit with an (R^2) value of 0.986 and a reduced χ^2 of 0.0042, confirming excellent agreement. The extracted full width at half maximum (FWHM) of the cross-correlation profile was 70.7 ± 1.2 fs, perfectly consistent with the expected convolution width of two ∼50 fs pulses, indicating that the holographic steering process and wedge-based delay generation introduce negligible additional temporal broadening or pulse distortion.

While the full holographic scan spans a 2.3 ps temporal window, figure 6 presents a magnified view of the central 276 fs interaction region in order to resolve the discrete temporal sampling intervals. The clearly distinguishable sampling points within the fitted Gaussian envelope confirm that the 17.1 mm lateral holographic sweep accurately translates into a highly linear temporal step size of 4.6 fs without requiring any mechanical translation stage. Furthermore, the absence of observable asymmetry or temporal distortion in the fitted cross-correlation profile experimentally validates the low-dispersion nature of the proposed all-optical delay architecture. The temporal delay values predicted from the wedge-based geometrical model showed excellent agreement with the experimentally measured SHG/SFG cross-correlation calibration, further validating the accuracy of the holographic delay generation mechanism.

4. Conclusion

In conclusion, we have successfully developed and validated an all-optical, mechanical-stage-free pump–probe methodology that eliminates the need for mechanical translation stages. By integrating a SLM into a novel hybrid temporal delay architecture, we have replaced instability-prone mechanical delay lines

with a purely digital holographic scanning mechanism. The implementation of the 4 f optical relay imaging system was crucial to this design; it actively compensated for the angular deviation induced during diffractive beam steering, ensuring stable spatiotemporal beam overlap at the focal plane without any lateral walk-off. This spatiotemporal wavefront engineering has enabled a rapid, automated 2.3 ps temporal scan with a high temporal sampling step of 4.6 fs. By providing exceptional spatial pointing stability and inherently robust interferometric precision, this holographic approach establishes a highly stable platform that mitigates the limitations associated with mechanical delay stages. Ultimately, this system demonstrates a promising alternative architecture for ultrafast optical instrumentation, opening promising pathways for phase-sensitive nonlinear diagnostics, coherent control experiments, and advanced ultrafast spectroscopy. Although the current hardware configuration demonstrates a fully mechanical-stage-free temporal scan window of 2.3 ps, this all-optical framework is highly adaptable. For experimental targets requiring delays of hundreds of picoseconds, the system can be easily supplemented with static coarse delay media (such as glass blocks) in the probe channel to shift the high-resolution holographic scanning window to any desired timeframe. However, the insertion of thick dispersive media would necessitate external dispersion pre-compensation (e.g. using a prism or grating compressor) to maintain transform-limited pulse durations. Furthermore, the absolute temporal range and step resolution can be scaled accordingly by modifying the wedge geometry or computationally increasing the number of holographic scan steps, highlighting the scalability and adaptability of the proposed digital architecture. Quantitative centroid tracking demonstrated a maximum centroid separation of only 14.0 μm, while the spatial overlap efficiency remained above 97.0% throughout the entire 2.3 ps holographic scan window, confirming highly stable spatiotemporal beam overlap.

Acknowledgments

This work was partially supported by TUBITAK 3501 (Project No. 120F002) and a TUBITAK-BIDEB grant (No. 2219-1059B192302459). We thank the late H. Schuessler for providing access to the SIBOR Laboratory facilities at Texas A&M University, where a portion of our experimental work was carried out.

Data availability statement

All data that support the findings of this study are included within the article (and any supplementary files).

Conflicts of interest

The authors declare no conflict of interest.

ORCID iD

Gamze Kaya 0000-0001-6660-0816

References

[1] Polli D, Lüer L and Cerullo G 2007 High-time-resolution pump-probe system with broadband detection for the study of time-domain vibrational dynamics *Rev. Sci. Instrum.* **78** 103108
[2] Tamaki R, Suzuki M, Kusaba S, Takeda J and Katayama I 2023 Ultrafast pump-probe spectroscopy via chirped-pulse up-conversion with dispersion compensation *Opt. Express* **31** 40142–50
[3] Velsink M C, Illienko M, Chaudhary K and Witte S 2025 Improving signal-to-noise ratios in pump-probe spectroscopy on light-sensitive samples by adapting pulse repetition rates *Opt. Express* **33** 23632–44
[4] Maiuri M, Garavelli M and Cerullo G 2020 Ultrafast spectroscopy: state of the art and open challenges *J. Am. Chem. Soc.* **142** 3–15
[5] Basov D N, Fogler M M and García de Abajo F J 2016 Polaritons in van der Waals materials *Science* **354** aag1992
[6] Zhang Q, Hu G, Ma W, Li P, Krasnok A, Hillenbrand R, Alù A and Qiu C W 2021 Interface nano-optics with van der Waals polaritons *Nature* **597** 187–95
[7] Sunku S S *et al* 2018 Photonic crystals for nano-light in moiré graphene superlattices *Science* **362** 1153–6

[8] Wilson N P, Yao W, Shan J and Xu X 2021 Excitons and emergent quantum phenomena in stacked 2D semiconductors *Nature* **599** 383–92
[9] Roushan P, Seo J, Parker C V, Hor Y S, Hsieh D, Qian D, Richardella A, Hasan M Z, Cava R J and Yazdani A 2009 Topological surface states protected from backscattering by chiral spin texture *Nature* **460** 1106–9
[10] Mauclair C, Najih B, Comte V, Bourquard F and Delaigue M 2025 Dynamic spatial beam shaping for ultrafast laser processing: a review *Opto-Electron. Sci.* **4** 250002–1–30
[11] Dönges S A, Khatib O, O'Callahan B T, Atkin J M, Park J H, Cobden D and Raschke M B 2016 Ultrafast nanoimaging of the photoinduced phase transition dynamics in VO2 *Nano Lett.* **16** 3029–35
[12] O'Callahan B T, Jones A C, Hyung Park J, Cobden D H, Atkin J M and Raschke M B 2015 Inhomogeneity of the ultrafast insulator-to-metal transition dynamics of VO2 *Nat. Commun.* **6** 6849
[13] Plankl M *et al* 2021 Subcycle contact-free nanoscopy of ultrafast interlayer transport in atomically thin heterostructures *Nat. Photon.* **15** 594–600
[14] Siday T *et al* 2022 Ultrafast nanoscopy of high-density exciton phases in WSe2 *Nano Lett.* **22** 2561–8
[15] Schibli T R, Kim J, Kuzucu O, Gopinath J T, Tandon S N, Petrich G S, Kolodziejski L A, Fujimoto J G, Ippen E P and Kaertner F X 2003 Attosecond active synchronization of passively mode-locked lasers by balanced cross correlation *Opt. Lett.* **28** 947–9
[16] Zhao Z, Kravtsov V, Wang Z, Zhou Z, Dou L, Huang D, Wang Z, Cheng X, Raschke M B and Jiang T 2025 Applications of ultrafast nano-spectroscopy and nano-imaging with tip-based microscopy *eLight* **5** 1
[17] Davis J A, Cottrell D M, Campos J, Yzuel M J and Moreno I 1999 Encoding amplitude information onto phase-only filters *Appl. Opt.* **38** 5004–13
[18] Davis J A, Cottrell D M, Lilly R A and Connely S W 1989 Multiplexed phase-encoded lenses written on spatial light modulators *Opt. Lett.* **14** 420–2
[19] Kaya N, Kaya G, Strohaber J, Zhou J, Kolomenskii A and Schuessler H 2021 Diffractive multifocal lenses by computer-generated holograms *Opt. Eng.* **60** 055107
[20] Keskin A, Kaya G, Kaya N, Strohaber J, Kolomenskii A A and Schuessler H A 2024 Dynamic control of airy beams using real-time phase-amplitude encoding on a spatial light modulator *Optics* **5** 581–94
[21] Kuang Z, Perrie W, Leach J, Sharp M, Edwardson S P, Padgett M, Dearden G and Watkins K G 2008 High throughput diffractive multi-beam femtosecond laser processing using a spatial light modulator *Appl. Surf. Sci.* **255** 2284–9
[22] Sanner N, Huot N, Audouard E, Larat C, Huignard J-P and Loiseaux B 2005 Programmable focal spot shaping of amplified femtosecond laser pulses *Opt. Lett.* **30** 1479–81
[23] Yang Y, Forbes A and Cao L 2023 A review of liquid crystal spatial light modulators: devices and applications *Opto-Electron. Sci.* **2** 230026–1–29
[24] Salter P S and Booth M J 2019 Adaptive optics in laser processing *Light Sci. Appl.* **8** 110
[25] Cumming B P, Turner M D, Schröder-Turk G E, Debbarma S, Luther-Davies B and Gu M 2014 Adaptive optics enhanced direct laser writing of high refractive index gyroid photonic crystals in chalcogenide glass *Opt. Express* **22** 689–98
[26] Jesacher A and Booth M J 2010 Parallel direct laser writing in three dimensions with spatially dependent aberration correction *Opt. Express* **18** 21090–9
[27] Kaya G, Keskin A, Dong J, Zhou J, Kolomenskii A A, Schuessler H A and Kaya N 2026 Dynamic control of laser filamentation with holographically generated Airy beams *Optik* **348** 172706
[28] Kaya G, Keskin A, Gökçen S and Kaya N 2026 Real-time generation of spatially controlled and angle-adjustable Airy beams using phase-only holography *Can. J. Phys.* **104** 1–5
[29] Kaya G, Kaya N, Strohaber J, Hart N A, Kolomenskii A A and Schuessler H A 2016 Nonadiabatic molecular alignment of linear molecules probed by strong-field ionization yields of photoelectrons *Appl. Phys. B* **122** 288
[30] Kaya N, Kaya G, Strohaber J, Kolomenskii A A and Schuessler H A 2016 Effect of circularly polarized femtosecond laser pulses on alignment dynamics of linear molecules observed by strong-field photoelectronyields *Eur. Phys. J. D* **70** 224
[31] Kaya N, Kaya G, Sayrac M, Boran Y, Anumula S, Strohaber J, Kolomenskii A A and Schuessler H A 2016 Probing nonadiabatic molecular alignment by spectral modulation *Opt. Express* **24** 2562–76
[32] Kaya N 2017 Field-free molecular alignment control of filamentation *Turkish J. Phys.* **41** 196–202
[33] Vaughan J C, Hornung T, Feurer T and Nelson K A 2005 Diffraction-based femtosecond pulse shaping with a two-dimensional spatial light modulator *Opt. Lett.* **30** 323–5
[34] Weiner A M 2000 Femtosecond pulse shaping using spatial light modulators *Rev. Sci. Instrum.* **71** 1929–60